Semi-classical approach to compute RABBITT traces in multi-dimensional complex field distributions

M. Lucchini,[1,*] **A. Ludwig,**[1] **L. Kasmi,**[1] **L. Gallmann,**[1,2] **and U. Keller**[1]

[1]*Department of Physics, ETH Zurich, CH-8093 Zürich, Switzerland*
[2]*Institute of Applied Physics, University of Bern, CH-3012 Bern, Switzerland*
[*]*mlucchini@phys.ethz.ch*

Abstract: We present a semi-classical model to calculate RABBITT (Reconstruction of Attosecond Beating By Interference of Two-photon Transitions) traces in the presence of a reference infrared field with a complex two-dimensional (2D) spatial distribution. The evolution of the electron spectra as a function of the pump-probe delay is evaluated starting from the solution of the classical equation of motion and incorporating the quantum phase acquired by the electron during the interaction with the infrared field. The total response to an attosecond pulse train is then evaluated by a coherent sum of the contributions generated by each individual attosecond pulse in the train. The flexibility of this model makes it possible to calculate spectrograms from non-trivial 2D field distributions. After confirming the validity of the model in a simple 1D case, we extend the discussion to describe the probe-induced phase in photo-emission experiments on an ideal metallic surface.

References and links

1. M. Ferray, A. L'Huillier, X. F. Li, L. A. Lomprk, G. Mainfray, and C. Manus, "Multiple-harmonic conversion of 1064 nm radiation in rare gases," J. Phys. B: At. Mol. Opt. Phys. **21**, L31–L35 (1988).
2. A. LHuillier, K. J. Schafer and K. C. Kulander, "Higher-order harmonic generation in xenon at 1064 nm: the role of phase matching," Phys. Rev. Lett. **66**, 2200 (1991).
3. F. Krausz and M. Ivanov, "Attosecond physics," Rev. Mod. Phys. **81**, 163–234 (2009).
4. L. Gallmann, C. Cirelli, and U. Keller, "Attosecond science: recent highlights and future trends," Ann. Rev. Phys. Chem. **63**, 447-469 (2012).
5. S. R. Leone, C. W. McCurdy, J. Burgdorfer, L. S. Cederbaum, Z. Chang, N. Dudovich, J. Feist, C. H. Greene, M. Ivanov, R. Kienberger, U. Keller, M. F. Kling, Z. Loh, T. Pfeifer, A. N. Pfeiffer, R. Santra, K. Schafer, A. Stolow, U. Thumm. and M. J. J. Vrakking, "What will it take to observe processes in 'real time'?" Nat. Photonics **8**, 162–166 (2014).
6. P. M. Paul, E. S. Toma, B. Breger, G. Mullot, F. Augé, Ph. Balcou, H. G. Muller, and P. Agostini, "Observation of a train of attosecond pulses from high harmonic generation," Science **292**, 1689 (2001).
7. M. Hentschel, R. Kienberger, C. Spielmann, G. Reider, N. Milosevic, T. Brabec, P. Corkum, U. Heinzmann, M. Drescher, and F. Krausz, "Attosecond metrology," Nature, **414**, 509–513 (2001).
8. M. Schultze, M. Fieß, N. Karpowicz, J. Gagnon, M. Korbman, M. Hofstetter, S. Neppl, A. L. Cavalieri, Y. Komninos, Th. Mercouris, C. A. Nicolaides, R. Pazourek, S. Nagele, J. Feist, J. Burgdörfer, A. M. Azzeer, R. Ernstorfer, R. Kienberger, U. Kleineberg, E. Goulielmakis, F. Krausz, and V. S. Yakovlev, "Delay in photoemission," Science **328**, 1658 (2010).

9. K. Klünder, J. M. Dahlström, M. Gisselbrecht, T. Fordell, M. Swoboda, D. Guénot, P. Johnsson, J. Caillat, J. Mauritsson, A. Maquet, R. Taïeb, and A. L'Huillier, "Probing single-photon ionization on the attosecond time scale," Phys. Rev. Lett. **106**, 143002 (2011).
10. J. Itatani, F. Quéré, G. L. Yudin, M. Yu. Ivanov, F. Krausz, and P. B. Corkum, "Attosecond streak camera," Phys. Rev. Lett. **88**, 173903 (2002).
11. H. G. Muller, "Reconstruction of attosecond harmonic beating by interference of two-photon transitions," Appl. Phys. B **74**, s17–s21 (2002).
12. A. L. Cavalieri, N. Müller, Th. Uphues, V. S. Yakovlev, A. Baltuška, B. Horvath, B. Schmidt, L. Blümel, R. Holzwarth, S. Hendel, M. Drescher, U. Kleineberg, P. M. Echenique, R. Kienberger, F. Krausz, and U. Heinzmann, "Attosecond spectroscopy in condensed matter," Nature **449**, 1029 (2007).
13. S. Neppl, R. Ernstorfer, E. M. Bothschafter, A. L. Cavalieri, D. Menzel, J. V. Barth, F. Krausz, R. Kienberger, and P. Feulner, "Attosecond time-resolved photoemission from core and valence states of magnesium," Phys. Rev. Lett. **109**, 087401 (2012).
14. R. Locher, L. Castiglioni, M. Lucchini, M. Greif, L. Gallmann, J. Osterwalder, M. Hengsberger, and U. Keller,"Attosecond interferometry unravels complex delays in photoemission from solids," arXiv:1403.5449 [cond-mat.other].
15. Y. Mairesse and F. Quéré, "Frequency-resolved optical gating for complete reconstruction of attosecond bursts," Phys. Rev. A **71**, 011401(R) (2005).
16. J. Gagnon, E. Goulielmakis, and V. S. Yakovlev,"The accurate FROG characterization of attosecond pulses from streaking measurements," Appl. Phys. B **92**, 25 (2008).
17. H. R. Telle, G. Steinmeyer, A. E. Dunlop, J. Stenger, D. H. Sutter, and U. Keller, "Carrier-envelope offset phase control: a novel concept for absolute optical frequency measurement and ultrashort pulse generation," Appl. Phys. B **69**, 327–332 (1999).
18. A. D. Rakić, A. B. Djurišic, J. M. Elazar, and M. L. Majewski, "Optical properties of metallic films for vertical-cavity optoelectronic devices," Appl. Opt. **37**, 5271–5283 (1998).
19. R. Courths and S. Hüfner, "Photoemission experiments on copper," Phys. Rep. **112**(2), 53–171 (1984).

1. Introduction

The discovery of coherent extreme-ultraviolet (XUV) generation with an intense few-cycle infrared (IR) pulse in a gas target, provided a new tool to access electron dynamics occurring on an attosecond time scale (1 as = 1×10^{-18} s) [1, 2]. Many interesting pioneering experiments have already been performed [3–5]. Single attosecond pulses (SAPs) [6] and attosecond pulse trains (APTs) [7] have been employed to resolve single photoionization delays in atoms [8, 9] using attosecond streaking [10] and RABBITT [6, 11]. These pioneering studies motivate the interest of the community to move towards more complex systems, with particular attention to solid state samples. So far, photoemission delays in solids have been studied with single attosecond pulses revealing short delays between the relative photoemission of core levels and valence band in W(110) and Mg(0001) crystals [12, 13]. In these experiments, the strong reference IR field needed to perform a streaking measurement ($\sim 1 \times 10^{12}$ W/cm^2) limits the applicability of the technique to relatively high photon energies where the secondary electron background is reduced. RABBITT measurements employing APTs, on the other hand, can be performed with considerably lower IR intensities ($\sim 1 \times 10^{11}$ W/cm^2), thus enabling to study the dynamics of weaker bound electrons. Recently, energy-dependent photoemission delays in the ionization of valence band electrons of Ag(111) and Au(111) crystals have been recorded with the RABBITT technique [14], showing a non-trivial behavior that cannot be explained by a model based only on transport phenomena.

In contrast to a gas target additional effects need to be taken into account in condensed matter, such as the reflection and refraction of the IR field at the surface of the sample. A noble metal surface, for example, exhibits a high reflection coefficient for the IR field and thus behaves as an almost perfect mirror. As a consequence, the field that interacts with the electrons during the pump and probe experiment is not simply formed by the probing IR pulse, but rather by the interference of incident and reflected light at the surface, which not only depends on the properties of the target, but also on the reflection and detection geometry. We therefore need to be able to distinguish between this *probe-induced* phase from the physical process under

study. Here, we introduce a semi-classical model to describe RABBITT traces with a complex two-dimensional (2D) field distribution. Starting from the streaking traces produced by the individual pulses in the train, we solve the classical equation of motion for a charged particle in an external field and attribute to each electron a "quantum phase" [15, 16]. This enables us to simply add all the contributions and finally reconstruct the RABBITT spectrogram as an interference of streaking traces. The advantage of this model is that it is easy to extend the calculations to complex 2D field distributions, *e.g.* the one created by the interference of an incoming and reflected wave. In Section 2, we present the model and apply it to a standard 1D problem of photoionization of an atomic gas. Section 3 then extends the model to a 2D field distribution. The results allows for a detailed analysis of the influence of the detection geometry in a 2D-IR transient grating, which is discussed in Section 4. Section 5 contains the conclusions.

2. Calculation of a RABBITT trace from the single pulse response

In this section we will show how to calculate a spectrogram for the case of an attosecond pulse train excitation. The electron spectra are obtained performing a coherent sum of the electron bursts generated by the individual attosecond pulses in the train. Here we will consider the problem of a rare gas atom ionized by the XUV radiation in the presence of a delayed IR pulse. For simplicity we will treat the case where both the IR and the XUV fields are linearly polarized and with polarization axes oriented along the *y*-axis towards the electron detection. We then can directly compare our results with the analytical solution given in [15,16].

We consider an XUV SAP defined by the electric field $E_{SAP}(t)$, with a Gaussian pulse envelope and a center frequency ω_c:

$$E_{SAP}(t) = e^{-\frac{t^2}{2\sigma^2}} \cdot \cos(\omega_c t) \tag{1}$$

where σ determines the FWHM pulse duration: $\sigma = \frac{FWHM}{2\sqrt{2\ln(2)}}$. Our goal is to calculate how the photoelectron energy will change during a pump-probe measurement where such a SAP ionizes the atoms in the presence of a few-femtosecond intense IR pulse. We assume that the center frequency of the pulse is high enough, such that the photoionization cross section does not depend on frequency. Thus, when the IR field is turned off, we can assume that the spectrum of the photoelectrons will be a replica of the photon spectrum shifted by the ionization potential of the target, I_p. In the case of a SAP with a Gaussian pulse envelope, the photon spectrum is defined by:

$$\hat{E}_{SAP}(\omega) = \frac{1}{2}\sqrt{2\pi}\sigma e^{-\frac{\sigma^2}{2}(\omega - \omega_c)^2}. \tag{2}$$

Assuming a semi-classical model and an placing our reference frame on the atom, *i.e.* the XUV-excited electron starts at $(x,y,z) = (0,0,0)$, we will describe its dynamics in the presence of the IR field as follows:

$$\frac{d^2}{dt^2}y(t) = -\frac{e}{m_e}E_y^{IR}(y,t-\tau), \quad \forall t \geq t_{ion} \tag{3}$$

where τ is the pump-probe delay, e and m_e are the charge ($e > 0$) and the mass of the electron, respectively. The time t_{ion} is the exact moment when the electron is excited into the continuum. We can treat this 1D problem taking into account only the *y*-component of the IR field:

$$\mathbf{E}^{IR}(y,t) = E_y^{IR}(y,t) \cdot \mathbf{u}_y = E_0\, e^{-\frac{y^2}{2\sigma_s^2}}\, e^{-\frac{t^2}{2\sigma_t^2}} \cos\left(\omega_0 t - \varphi_{in}\right) \cdot \mathbf{u}_y \tag{4}$$

where ω_0 is the driving laser frequency, $\mathbf{y}$ is the position vector, σ_t/σ_s define pulse duration/dimension of the IR beam with phase φ_{in} and polarized along the y axis defined by unity vector $\mathbf{u}_y$. Substituting this IR field definition into Eq. (3) and solving the differential equation one can obtain the electron trajectories and velocities as a function of the pump-probe delay τ. As an example, Fig. 1 shows the electron trajectories and velocities for a fixed delay $\tau = 0$ fs in the case of ionization of argon atoms.
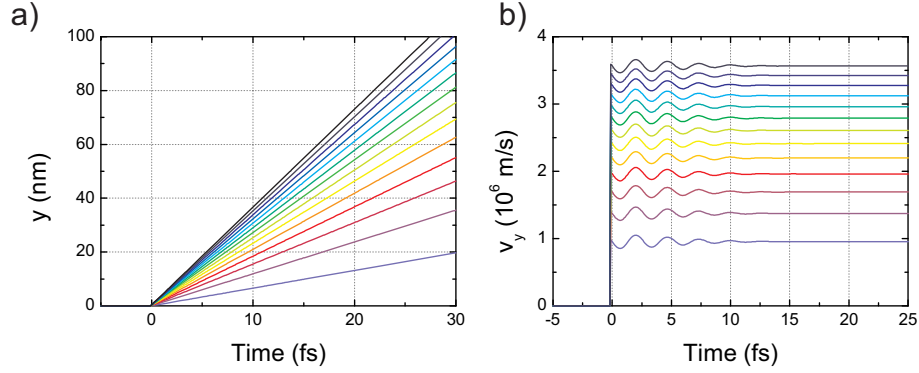

Fig. 1. Solution of the classical electron trajectories for a set of electrons photo-emitted from an argon atom by an attosecond pulse in the presence of an IR field at delay $\tau = 0$ fs. (a) Trajectories of selected electrons emitted in the positive y direction. (b) Velocities as a function of time. Parameters used in the calculations: XUV time duration 300 as, center wavelength equal to the 21st harmonic of the fundamental IR beam with wavelength $\lambda_0 = 796$ nm. The time duration of the IR pulse is 12 fs and the intensity is 5×10^{11} W/cm^2.

Since the typical time duration of the IR pulses are longer than the SAP, we will neglect in the following the temporal extension of the XUV pulse and assume that all the spectral components of the photoelectron burst are created at the same instant of time t_{ion}. This assumption is not valid in case the XUV pump pulse is chirped. We would like to stress that this constraint is easy to relax, but it is not necessary for the analysis reported in this work.

By repeating the calculations presented in Fig. 1 for different time delays between the IR probe and XUV pump pulse we can obtain the spectrogram (Fig. 2(a)), which represents a streaking trace. In order to calculate the response of an APT this is not enough. We need to calculate the phase that every electron acquires during the interaction with the IR field and perform a coherent sum of all the contributions. The "quantum phase" acquired by the electrons can be written as [15, 16] (atomic units):

$$\varphi(v_f, \tau) = \int_{t_{ion}}^{\infty} \left(\mathbf{v}_f \cdot \mathbf{A}(\mathbf{r}, t - \tau) + \frac{\mathbf{A}^2(\mathbf{r}, t - \tau)}{2} \right) dt, \tag{5}$$

where $\mathbf{v}_f = v_f \cdot \mathbf{u}_{v_f}$ is the final velocity of the electron, $\mathbf{r} = [x, y]$ describes the trajectory and $\mathbf{A}(\mathbf{r}, t)$ is the IR vector potential acting on the electron during its classical motion in the continuum. The final velocity $\mathbf{v}_f$ is related to the instantaneous momentum $\mathbf{p}$ by:

$$\mathbf{p}(\mathbf{r}, t) = \mathbf{v}_f + \mathbf{A}(\mathbf{r}, t). \tag{6}$$

Equation (5) then becomes:

$$\varphi(v_f, \tau) = \int_{t_{ion}}^{\infty} \left(\mathbf{p}(\mathbf{r}, t - \tau) \cdot \mathbf{A}(\mathbf{r}, t - \tau) - \frac{\mathbf{A}^2(\mathbf{r}, t - \tau)}{2} \right) dt. \tag{7}$$

The equation of motion (Eq. (3)) determines the electron trajectories and velocities which are then used in Eq. (7) to evaluate the phase $\varphi(v_f, \tau)$. The response of a single electron in amplitude and phase can be defined as:

$$SAP(v_f, \tau) \triangleq S(v_f, \tau)\, e^{i\varphi(v_f, \tau)}. \tag{8}$$

where $|S(v_f, \tau)|^2$ is the probability to detect an electron with final velocity v_f for a given delay τ, and $\varphi(v_f, \tau)$ is its associated quantum phase calculated by Eq. (7). The results in the case of ionization of an argon atom by a 300-as XUV pulse are displayed in Fig. 2.
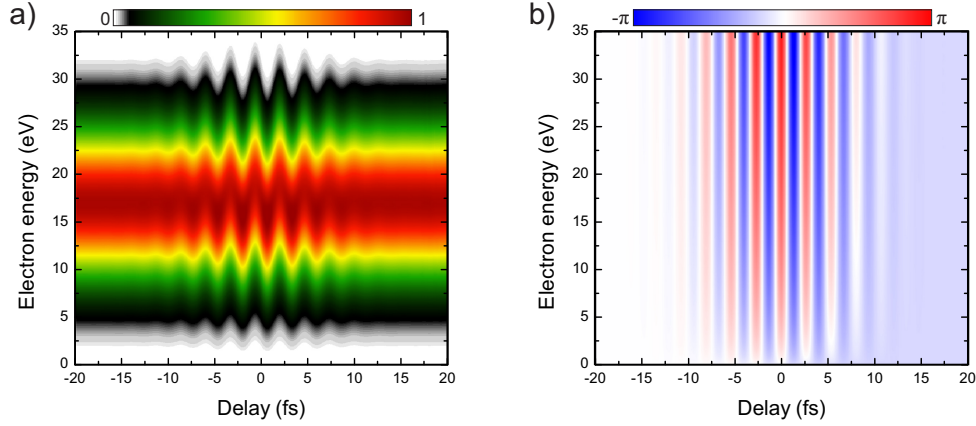

Fig. 2. (a) and (b), calculated intensity and phase of the photoelectrons as a function of delay τ between IR and XUV pulse, respectively. Positive delays means that the IR pulse arrives later than the XUV pulse. Calculation parameters are the same as in Fig. 1. The quantum phase in (b) has been evaluated by Eq. (7).

The response for an attosecond pulse train, $APT(v_f, \tau)$, can now be calculated starting from $SAP(v_f, \tau)$ and following the properties of the Fourier transform as we will describe in the following.

First we consider the static situation, when the probe IR field is not present and the XUV pump pulse is given by an attosecond pulse train with a Gaussian envelope $G(t)$. In the time domain we can write:

$$E_{APT}(t) = G(t) \cdot P(t), \tag{9}$$

where $P(t)$ is an infinite train of attosecond pulses. The Fourier transform of $APT(t)$ is then given by:

$$\hat{E}_{APT}(\omega) = F\{E_{APT}(t)\} = F\{G(t) \cdot P(t)\} = \hat{G}(\omega) * \hat{P}(\omega). \tag{10}$$

The symbol $*$ represents the convolution and $\hat{G}(\omega)$ the Fourier transform of the Gaussian envelope. In analogy with Eq. (2), $\hat{G}(\omega)$ is given by:

$$\hat{G}(\omega) = \frac{1}{2}\sqrt{2\pi}\sigma_{env} e^{-\frac{\sigma_{env}^2 \omega^2}{2}}. \tag{11}$$

Due to the linearity of the Fourier operator and the "shift theorem", the Fourier transform of the infinite train can be written as the sum of the transforms of the single elements constituting the train times a proper linear phase term which takes into account for the relative delays between

the pulses:

$$\hat{P}(\omega) = F\{P(t)\} = F\{\sum_{n=-\infty}^{+\infty} p(t - n\frac{T}{2})\} = \sum_{n=-\infty}^{+\infty} F\{p(t - n\frac{T}{2})\} \tag{12}$$

$$= \sum_{n=-\infty}^{+\infty} \hat{p}(\omega)e^{-i\omega n\frac{T}{2}}, \tag{13}$$

where $T = \frac{2\pi}{\omega_0}$ is the period of the IR field and n is an integer number. Figure 3 shows the spectrum of an attosecond pulse train $\hat{E}_{APT}(\omega)$ constructed with this procedure, starting from the definition of the SAPs in the train.
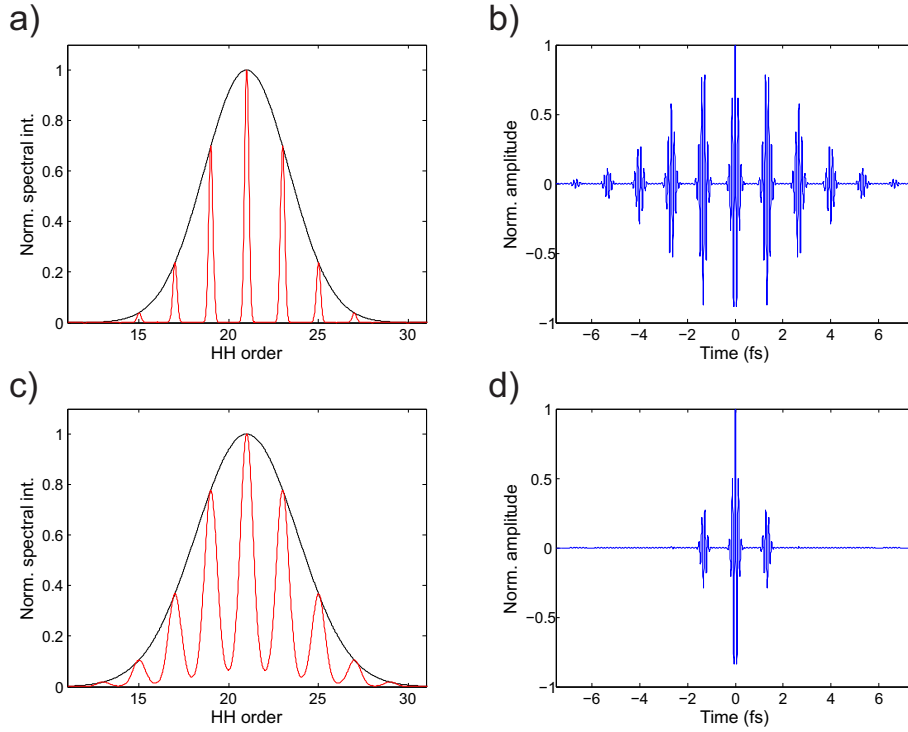

Fig. 3. Spectra of two different APTs (red lines) calculated starting from the spectrum of the SAP (black lines) as described in Eqs. (10), (11) and (13). Parameters used in the calculations: (a) $\sigma = 300$ as, $\sigma_{env} = 6$ fs; (c) $\sigma = 250$ as, $\sigma_{env} = 2$ fs (see Eqs. (2) and (11)). (b), (d) show the temporal behavior obtained by inverse Fourier transform of the red spectra in (a), (c) respectively.

Following the same procedure, it is easy to rewrite the total response when a delayed IR field is turned on. The RABBITT spectrogram $|APT(\omega, \tau)|^2$ can indeed be obtained by taking the frequency response of the system to the single pulse from Eq. (8) and exploiting the fact that the response of a subsequent pulse in the train will be exactly equal to the one of the previous pulse at a delay $\hat{\tau} = \tau \pm \frac{T}{2}$:

$$\hat{P}(\omega, \tau) = \sum_{n=-\infty}^{+\infty} SAP(\omega, \tau - n\frac{T}{2})e^{-i\omega n\frac{T}{2}} e^{-in\pi}. \tag{14}$$

The additional phase term $e^{-in\pi}$ takes into account the fact that the carrier-envelope phase (CEP) [17] of the attosecond pulses in the train exhibits a π-jump between subsequent pulses. Given that $T = \frac{2\pi}{\omega_0}$, we can finally write:

$$\hat{P}(\omega, \tau) = \sum_{n=-\infty}^{+\infty} SAP(\omega, \tau - n\frac{T}{2})e^{-i(\omega-\omega_0)n\frac{T}{2}} \tag{15}$$

Inserting Eq. (11) and Eq. (15) in Eq. (10) and calculating the convolution, we can obtain the spectrogram in the case of attosecond pulse trains, $APT(\omega, \tau) = \hat{G}(\omega, \tau) * \hat{P}(\omega, \tau)$. The result for the case presented in Fig. 2 is shown in Fig. 4. As expected, the interference between the
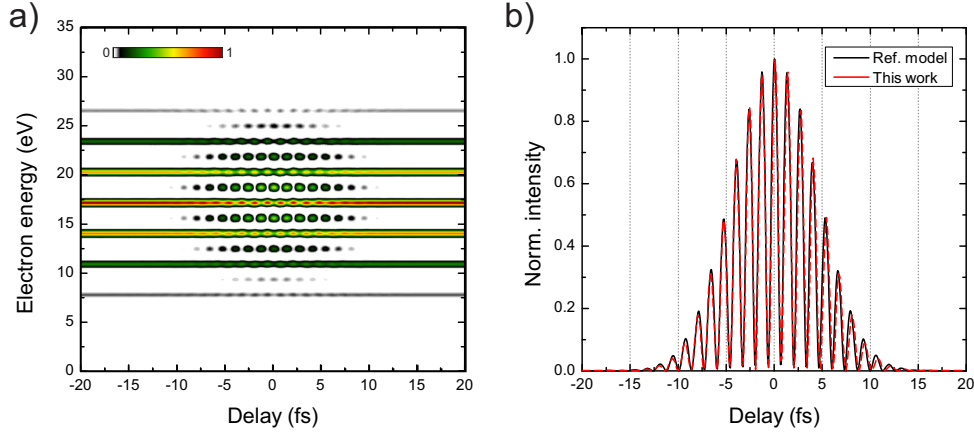

Fig. 4. (a) RABBITT trace obtained with the procedure described in the text starting from the SAP response of Fig. 2 and assuming an APT as the one in fig. 3(a)-(b). (b) comparison between the delay evolution of SB 22 at 18.2 eV extracted from the RABBITT trace calculated with the analytical formula of Eq. (2) in [15] (black curve) and extracted from the spectrogram in (a) (red-dashed curve).

different streaking traces manifests itself by the appearance of discrete peaks located at the position of odd harmonics of the fundamental frequency ω_0. When the IR and APT overlap, an oscillating sideband (SB) signal appears at the position of even harmonics between two main peaks. The SB signal can be interpreted in a full quantum model as arising from the interference of two quantum paths involving the absorption of photons from two neighboring harmonics and emission/absorption of an additional IR photon. These two pathways interfere in the SB signal producing an oscillation at twice the fundamental IR frequency ω_0. Figure 4(b) displays the comparison between the evolution of SB 22 calculated with the analytical integral of Eq. (2) in [15] and the model presented in this section. The agreement between the two models provides an additional sanity check of our method.

3. Generalization to a 2D field distribution

The method introduced in the previous section enables an easy extension to any 2D-IR field distribution. As an example, we will consider a RABBITT experiment performed by ionizing an ideal metal characterized by a complex energy dependent refractive index $\tilde{n}(\omega)$ as in [14], Locher et al. In the following, we will restrict our analysis to the geometry sketched in Fig. 5, where both the IR and XUV radiation are linearly polarized, propagate collinearly towards the metallic surface with p-polarization.
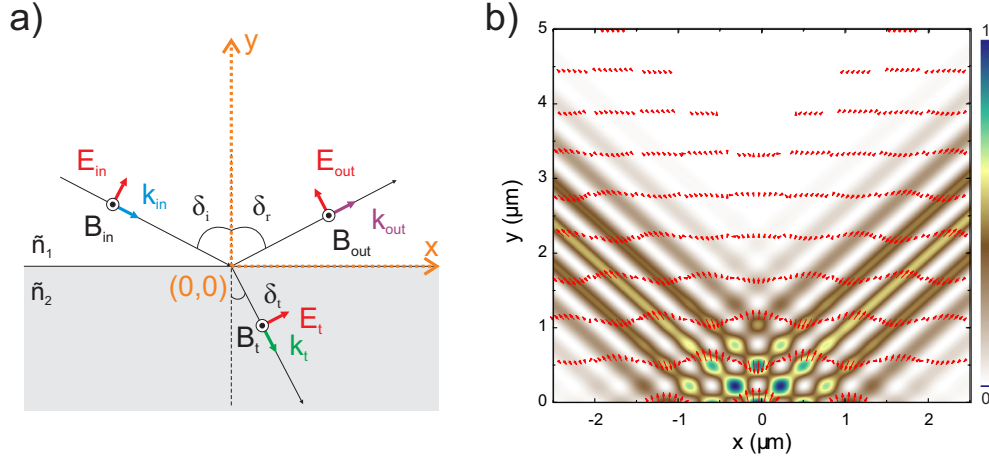
Fig. 5. (a) Reflection and refraction of a *p*-polarized light beam at a metal surface. The arrows indicate the positive direction chosen for the vectorial quantities under investigation. (b) Intensity map of the IR transient grating for the instant of time $t = 0$ fs and an incident angle $\delta_i = 45°$. The field distribution is calculated with Eq. (17) for an IR field reflected on a perfect copper surface. Parameters used in the calculation: center wavelength $\lambda_0 = 786$ nm, pulse duration: 10 fs, σ_s: 70 μm and an intensity of 5×10^{11} W/cm^2. The red arrows show the direction and magnitude of the total electric field for selected points in space.

Following the reference frame of Fig. 5, the IR field can be written as:

$$\mathbf{E}^{IR}(x,y,t-\tau) = \mathbf{E}^{IR}_{in}(x,y,t-\tau) + \mathbf{E}^{IR}_{out}(x,y,t-\tau), \tag{16}$$

where the incoming and outgoing waves are:

$$\begin{cases} \mathbf{E}^{IR}_{in}(x,y,t-\tau) = E_{in}\, e^{-\frac{(\mathbf{u}^{\perp}_{in}\cdot\mathbf{r})^2}{2\sigma_s^2}}\, e^{-\frac{(\mathbf{u}^{\parallel}_{in}\cdot\mathbf{r}/c-t)^2}{2\sigma_t^2}} \cos(\mathbf{k}_{in}\cdot\mathbf{r} - \omega_0 t + \varphi_{in})\cdot\mathbf{u}^{\perp}_{in} \\[2ex] \mathbf{E}^{IR}_{out}(x,y,t-\tau) = E_{out}\, e^{-\frac{(\mathbf{u}^{\perp}_{out}\cdot\mathbf{r})^2}{2\sigma_s^2}}\, e^{-\frac{(\mathbf{u}^{\parallel}_{out}\cdot\mathbf{r}/c-(t-\beta))^2}{2\sigma_t^2}} \cos(\mathbf{k}_{out}\cdot\mathbf{r} - \omega_0 t + \varphi_{out})\cdot\mathbf{u}^{\perp}_{out}. \end{cases} \tag{17}$$

Here $\mathbf{r}$ is the position vector and σ_s defines the spatial dimensions of the beam. $\mathbf{k}_{in/out}$ is the k-vector of the incoming/outgoing wave, while $\mathbf{u}^{\perp/\parallel}_{in/out}$ is an unity vector perpendicular/parallel to $\mathbf{k}_{in/out}$. Amplitude and phase of $\mathbf{E}^{IR}_{out}$ are calculated starting form the Fresnel equations with the following assumptions:

$$A_{out}(\omega) \simeq A_{out}(\omega_0) = A_{in}\cdot|r_p(\omega_0,\delta_i)| \tag{18}$$

$$\varphi_{out}(\omega) = \varphi_{in} + \arg\{r_p(\omega,\delta_i)\} \simeq \varphi_{in} + \beta\omega + \beta_0, \tag{19}$$

where the complex reflection coefficient is given by:

$$r_p(\omega,\delta_i) = \frac{\tilde{n}_2(\omega)^2\cos(\delta_i) - \tilde{n}_1(\omega)\sqrt{\tilde{n}_2(\omega)^2 - \tilde{n}_1(\omega)^2\sin^2(\delta_i)}}{\tilde{n}_2(\omega)^2\cos(\delta_i) + \tilde{n}_1(\omega)\sqrt{\tilde{n}_2(\omega)^2 - \tilde{n}_1(\omega)^2\sin^2(\delta_i)}}. \tag{20}$$

δ_i is the angle of incidence for the IR beam with respect to the surface normal, $\tilde{n}_2(\omega)$ and $\tilde{n}_1(\omega)$ are the complex refractive indices of the two media at the interface. β_0 and β are the

two coefficients which define the linear expansion of the frequency dependent Fresnel phase, $\arg\{r_p(\omega, \delta_i)\}$ acquired after reflection. Figure 5(b) shows the 2D-transient grating that a 10-fs IR pulse with a lateral dimension $\sigma_s = 70 \ \mu$m creates at the moment of reflection on a copper metallic surface. For this example, the values for the complex refractive index of copper are taken from [18], Rakić et al.

In two dimensions, the equation of motion, Eq. (3), is replaced by the coupled system of equations:

$$\begin{cases} \frac{\partial^2}{\partial t^2} x(t) = -\frac{e}{m_e} E_x^{IR}(x, y, t - \tau) \\ \frac{\partial^2}{\partial t^2} y(t) = -\frac{e}{m_e} E_y^{IR}(x, y, t - \tau), \end{cases} \tag{21}$$

where the Cartesian components of the total IR field depend on angle of the incidence δ_i:

$$\begin{cases} E_x^{IR} = \left(E_{in}^{IR} - E_{out}^{IR} \right) \cos(\delta_i) \\ E_y^{IR} = \left(E_{in}^{IR} + E_{out}^{IR} \right) \sin(\delta_i) \end{cases} \tag{22}$$

As previously discussed, in order to obtain the RABBITT trace we have to evaluate the "quantum phase" in Eq. (7). Here the vector potential $\mathbf{A}(x, y, t) = -\int_{-\infty}^{t} \mathbf{E}(x, y, t') dt'$ is given by the sum of the vector potentials of the incoming and reflected waves. If we define the quantities $\mathbf{C}_{in} = -E_{in} \mathbf{u}_{in}^{\perp} e^{-\frac{(\mathbf{u}_{in}^{\perp} \cdot \mathbf{r})^2}{2\sigma_s^2}}$, $a = \mathbf{u}_{in}^{\parallel} \cdot \mathbf{r}$, $b = \sqrt{2}c\sigma_t$ and $d = \mathbf{k}_{in} \cdot \mathbf{r} + \varphi_{in}$, we can write the vector potential with the following analytical expression:

$$\mathbf{A}_{in} = \mathbf{C}_{in} \int_{-\infty}^{t} e^{-\frac{(a-ct)^2}{b^2}} \cos(d - \omega_0 t) \, dt \tag{23}$$

$$= \mathbf{C}_{in} \frac{b}{4c} e^{-\left(id + \frac{\omega_0 (4iac + b^2 \omega_0)}{4c^2} \right)} \sqrt{\pi} \left\{ e^{2id} \left[1 - \text{Erf} \left(\frac{2c(a - ct) - ib^2 \omega_0}{2bc} \right) \right] + \right.$$

$$\left. + e^{\frac{2ia\omega_0}{c}} \left[1 - \text{Erf} \left(\frac{2c(a - ct) + ib^2 \omega_0}{2bc} \right) \right] \right\}, \tag{24}$$

where Erf is the error function extended to the complex domain. $\mathbf{A}_{out}$ has the same form, but with amplitude and phase determined by the Fresnel equations. So, also in this 2D example, the RABBITT spectrogram can be computed starting from the definition of the IR field distribution and the solution of the classical electron trajectories as done in the previous section. When compared to the 1D problem, the main difference is that different RABBITT traces depend on the detection geometry. This will be discussed in the following section.

4. Effect of the field distribution on the electron phase

Following the method developed in the previous section, we can calculate a RABBITT spectrogram for electrons ionized by an APT at a metallic surface in the presence of a 2D IR grating. For the sake of simplicity, in this paper we will neglect any transmitted IR field in the solid sample and assume that the electrons are generated in an infinitely thin layer right below the surface. Therefore, with this assumption, we will consider only the electrons which are generated all at the same depth immediately below the surface. An analysis of transport properties of the carriers in the solid is beyond the scope of the present manuscript. Here, the focus is on applying the model to study the effect of the 2D-IR transient grating phase on the phase of the sideband signals in the RABBITT trace. In particular, we will focus on the dependence on the detection angle. It is worthy to point out that for the case of a noble metal with a high reflection coefficient for the IR field, electrons have to travel to the surface before being able to interact

with the femtosecond pulse. Including the finite generation depth of the electrons in the solid and the phase they acquire on propagation to the surface would in this case result in a reduction of the SB modulation contrast and in a shift of the SB phases. This shift does not depend on the properties of the IR transient grating, though, and only affects the reference phase φ_0 that we will introduce later in this section.

We consider a copper sample and solve the system of Eqs. (21) under the assumption that all the electrons are generated at the origin, $(x,y) = (0,0^-)$. If the IR lateral dimension is bigger than the XUV one, such that the IR intensity can be considered constant across the XUV radial profile, the final results are not affected by this assumption. For a given photon energy $\hbar\omega$ and initial angle θ with respect to the surface plane, the initial components of the electron velocity inside the solid can be written as:

$$\begin{cases} v_x^{in} = \sqrt{\frac{2}{m_e}}\sqrt{h\nu + E_b - E_{bvb}}\cos(\theta) \\ v_y^{in} = \sqrt{\frac{2}{m_e}}\sqrt{\sin^2(\theta)[h\nu + E_b] + \cos^2(\theta)E_{bvb}} \end{cases} \tag{25}$$

where E_b and E_{bvb} are the binding energy and the energy of the bottom of the valence band. In the present case, we took $E_b = -8.04$ eV and $E_{bvb} = -12.44$ eV [19] in order to represent ionization of the copper $3d$-valence band. In analogy to optical refraction of light at a discontinuity interface of the refractive index, due to the energy barrier in the y direction, different *external* angles θ' correspond to the same starting *internal* angle θ (Fig. 6).

If we focus on a SAP and solve the classical trajectories, we can access the final electron direction θ'_{fin} and energy $\hbar\omega$. So we can rewrite the SAP response as a function of energy, delay and angle by summing over all the contributions with different initial velocities v_{in} and angles θ which map to the same point in the *final* space:

$$SAP(\omega, \tau, \theta'_{fin}) = \sum_\theta \left(\sum_{v_{in}} \left(S(v_{in}, \tau, \theta)\, e^{i\varphi(v_{in}, \tau, \theta)} \right) \cdot \sin(\theta) \right) \tag{26}$$

where the factor $\sin(\theta)$ takes into account the increased scattering probability for electrons that travel in a direction more parallel to the surface. The spectrogram in the case of APTs can now be evaluated following Eq. (15) for each final angle. In this way, it is possible to evaluate the trace that a detector placed in the incidence plane with a certain angle γ from the normal will record. Figure 6 displays the RABBITT traces calculated for electrons collected by a detector with a $10°$ acceptance angle at $\gamma = 5°$, $45°$ and $75°$ for the 2D-IR transient grating formed in Fig. 5 ($\delta_i = 45°$). Even if the three traces look similar, they contain information about the different interaction of the electrons with the IR field. This information can be extracted by retrieving the phase of the oscillating sidebands in the traces.

For a given detection angle, the signal of sideband with order $2q$ is obtained by integrating the spectrogram in an energy window $\Delta E = 1$ eV around the energies of SBs 14 to 28. The phase of the SB signal is then extracted by fitting the data with the following function:

$$SB^{(2q)}(\tau) = \left[a_1 \cos^2\left(\omega_0(\tau - a_3) + \frac{\varphi_{in} + \varphi^{(2q)}}{2} \right) + a_2 \right] e^{-\left(\frac{\tau - a_3}{a_4}\right)^2} + a_5 \tag{27}$$

The additional Gaussian envelope in Eq. (27) is due to the fact that the sum over electrons emitted with different angles θ' decreases the contrast of the oscillating $2\omega_0$-signal. This background becomes more important for big detection angles, where the effect of the refraction at the surface is stronger.

Next we can compare the extracted energy-dependent phases $\varphi^{(2q)}$ with the Fresnel phase from the reflection on the surface. For reasons that will be clarified in the following, it is

convenient to write $\varphi^{(2q)}$ as equal to the sum of a constant offset plus a reflection phase $\varphi_R^{(2q)} = \varphi^{(2q)} - \varphi_0$. This offset is introduced by the choice of the temporal and spatial shapes of the IR and APT. If we put the initial phase of the IR field $\varphi_{in} = 0$, switch off the x-component of the IR electric field and look at electrons emitted in direction normal to the surface ($\theta = \theta' = 90°$), the motion of the negative charges will be driven only by the sum of the incident and reflected y-component of the IR electric field. In this case the relation between the reflection phase, $\varphi_R^{(2q)}$, and the Fresnel phase acquired by the reflected part of the IR pulse, $\varphi_{Fre}^{(2q)}$, becomes:

$$\varphi_R^{(2q)} = \frac{\varphi_{Fre}^{(2q)}}{2} \simeq \frac{\beta \omega_0 + \beta_0}{2} \tag{28}$$

Therefore, we can obtain the offset phase φ_0 performing this ideal experiment as $\varphi_0 = \varphi_m^{(2q)} - \varphi_{Fre}^{(2q)}/2$ and subtract its contribution from the analysis of the full calculations.

Figure 7 shows the final result. RABBITT traces are calculated for the detection angle γ adjusted with 5°-steps between 10° and 75°. Subsequently the reflection phases, $\varphi_R^{(2q)}$, are extracted from SB 14 to 28 removing the constant offset φ_0 from the phases extracted with the
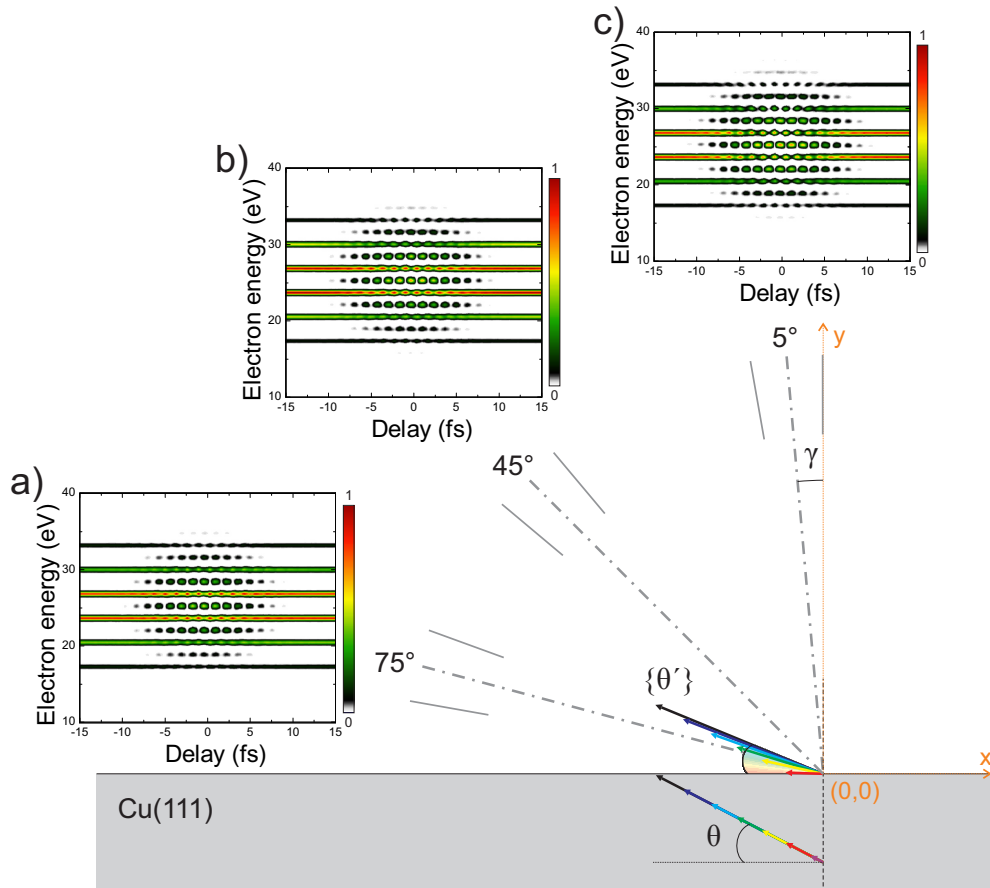

Fig. 6. (a)-(c), calculated RABBITT traces for electrons with final angle θ'_{fin} in a 10°-wide full acceptance angle centered at an angle $\gamma = 75°$, 45° and 5°, respectively. The APT is the same as Fig. 3(a)-(b). IR field parameters used in the calculations: same as Fig. 5(b).
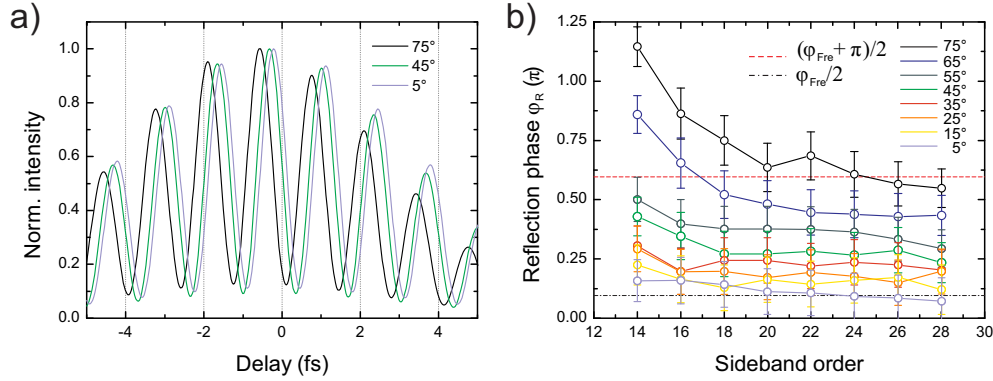
Fig. 7. (a) Fitting of SB 20 for three selected values of detection angle γ. The oscillating trace moves towards positive pump-probe delays for decreasing detection angles, which means a smaller measured phase $\varphi_m^{(2q)}$. b) Behavior of the reflection phase $\varphi_R^{(2q)}$ as a function of detection angle γ and SB order. For small angles (close to normal emission condition), the reflection phase equals half of the Fresnel phase, $\varphi_{Fre}/2$ (black dot-dashed line), while it approaches $\varphi_{Fre}/2 + \pi/2$ (red dashed line) for bigger angles when the influence of the x-component of the IR total field becomes stronger. The error bars in (b) represent the confidence interval of the fitting procedure on the retrieved phase.

fitting procedure $\varphi_m^{(2q)}$. As shown in Fig. 7(b), the reflection phase $\varphi_R^{(2q)}$ is strongly influenced by the detection angle. In particular, for detection close to normal emission, $\varphi_R^{(2q)}$ is approximately equal to half the Fresnel phase as expected. For small γ one collects mostly electrons with a starting velocity parallel to the y direction. Therefore the y-component of the IR electric field affects more the absolute value of the final electron momentum, while the x-component of the field mostly streaks the electrons angularly. In this limit one can easily go back to the more known quantum description of the RABBITT process and imagine that the electrons will, on average, interact with one IR photon of the incident beam (with phase equal to zero) and one of the reflected beam (with phase increased by φ_{Fre}), thus acquiring a final phase $\varphi_R = \varphi_{Fre}/2$. As clearly shown in Fig. 7(b), this picture is no longer valid when electrons are collected at a bigger angle with respect to the normal. Here the field component that can more efficiently modify the absolute value of the final momentum is the one parallel to the surface. A closer look at Eqs. (17) and (22) unravels that if the y component of the IR field E_y^{IR} oscillates as $\propto \cos(-\omega_0 t + \varphi_{Fre}/2)$, the x component, E_x^{IR}, should behave as $\propto -\sin(-\omega_0 t + \varphi_{Fre}/2)$. Thus the two components are phase-shifted by $\pi/2$. For big detection angles γ and low SB orders the refraction of the electrons at the surface is stronger and mixes different energetic components of the electron spectrum. This explains the observed deviation of the calculated phases from the value of $\varphi_{Fre}/2 + \pi/2$ in the case of slow electrons detected parallel to the surface.

We therefore can rewrite the reflection phase as a function of the Fresnel phase corrected by a coefficient $\alpha(\gamma)$, which takes the geometry of detection into account:

$$\varphi_R^{(2q)} \simeq \frac{\varphi_{Fre}}{\alpha(\gamma)} \tag{29}$$

From the discussion above, it follows that α is expected to be equal to 2 for normal detection and to decrease for smaller values of γ. Figure 8 shows the "geometry coefficient" α extracted directly from Fig. 7(b) by averaging over the SB order.
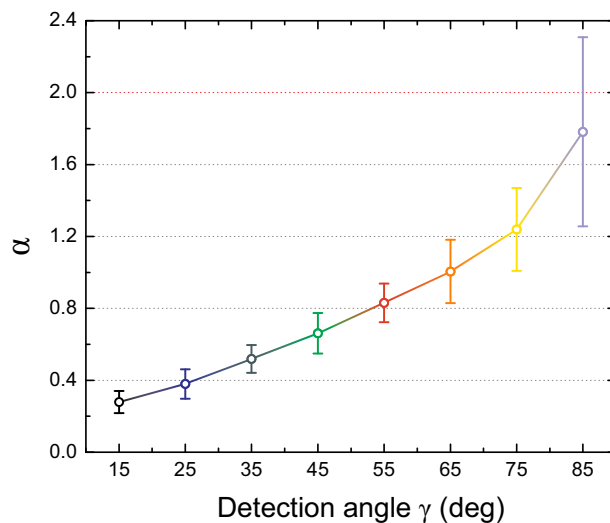
Fig. 8. Behavior of the "geometry coefficient" α (Eq. (29)) as a function of the detection angle γ extracted from the reflection phases $\varphi_R^{(2q)}$ of Fig. 7(b). Close to normal emission the reflection phase is almost half of the Fresnel phase and therefore α becomes $\simeq 2$. Electrons emitted parallel to the surface acquire a bigger phase during the interaction with the IR transient grating and thus α decreases.

5. Conclusion

In conclusion, we have demonstrated that it is possible to calculate RABBITT traces starting from the response of the single attosecond pulses constituting the train and treating the IR field dynamics with a classical model. The coherent sum of the individual responses is evaluated taking into account the "quantum phase" based on the semi-classical action and accumulated by the electrons during their interaction with the IR field. We verified the model for the simple case of ionization of a noble gas atom. The potential of the presented method lays in the fact that it can be easily generalized to multi-dimensional complex IR field distributions. As an example, we computed the RABBITT traces produced by a few-femtosecond IR pulse reflected from a perfect noble metal surface (*e.g.* copper crystal) and varied the detection angle for the photoelectrons. A detailed analysis of the phases extracted from the sideband signals shows that the final phase transferred from the IR 2D-transient grating to the photoelectrons strongly depends on the detection geometry. In particular, we were able to demonstrate that the intuitive photon picture, often used to describe RABBITT can be applied only for electrons emitted perpendicularly to the surface. For smaller emission angles the result deviates significantly from a total transferred phase equal to half the Fresnel phase as suggested by the simple photon picture. We believe that the presented method will provide an important tool to evaluate the IR induced phase in attosecond measurements on solid targets, thus enabling a correct extraction of photoemission delays. This will give direct access to the more fundamental attosecond ionization time delays.

Acknowledgment